Merging galaxy clusters: probing magnetism and particle acceleration over cosmic time

Di Gennaro, G.

CHAPTER

1

INTRODUCTION

1.1. Galaxy clusters

Galaxy clusters are the largest virialized structures in the Universe. They can contain more than a thousand galaxies within a radius of $\sim 1-2$ Mpc. However, galaxies only represent a small percentage of the cluster's mass, which is about 10^{14-15} $M_\odot$. The bulk of the cluster mass is in the form of *dark matter* (70–80%), although its nature is still unknown. The remaining mass of a cluster, the *baryonic* content, is dominated by a dilute and hot plasma. This intracluster medium (ICM) fills the space in between the cluster member galaxies.

According to the current Cosmology (ΛCDM[1], where Λ refers to the cosmological constant and CDM stays for Cold Dark Matter), structure formation is thought to be a consequence of a hierarchical growth of small density fluctuations under the effect of gravity (e.g. Peebles, 1980; Coles & Chiang, 2000). Such variations could be produced by cosmic inflation, and are detected as temperature anisotropies in the cosmic microwave background (CMB), which maps the surface of last scattering between matter and radiation. In this framework, galaxy clusters are the latest structures to form, at the intersections of filaments in the cosmic web.

The gravitational collapse of the small fluctuations is usually studied via hydrodynamical cosmological simulations (e.g. Illustris, Fig. 1.1, Vo-

[1]The values for the density contrast of the cosmological constant and of the matter are $\Omega_\Lambda = 0.7$ and $\Omega_m = 0.3$, respectively.

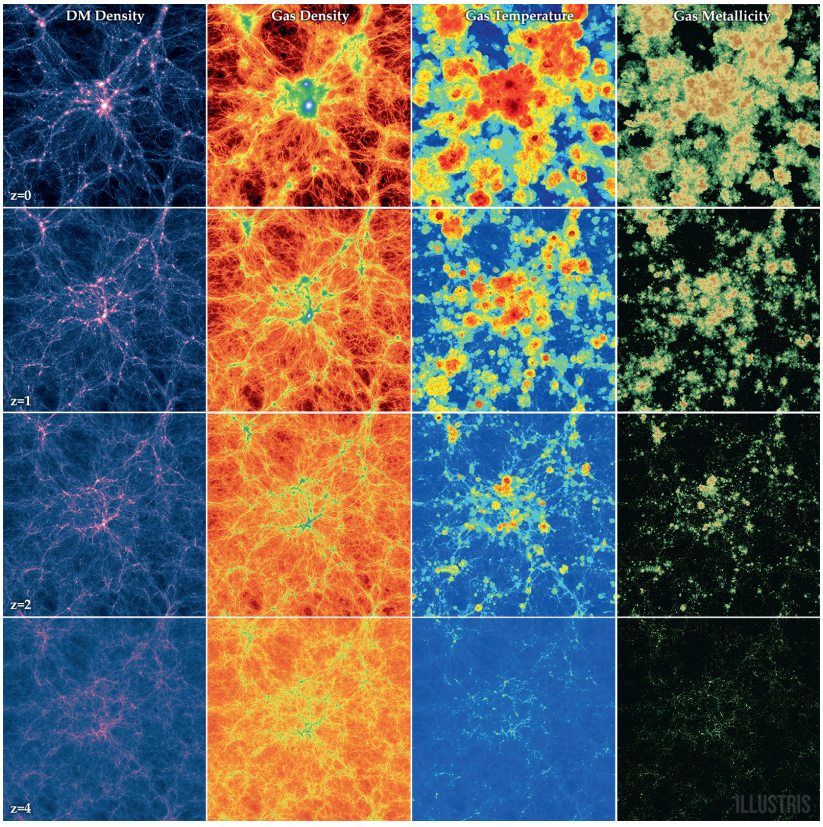

Figure 1.1: Illustris simulation of the redshift evolution of the most massive cluster at $z = 0$ from $z = 4$ (the box size is 106.5 Mpc). The four columns show four quantities from the of the simulation (from left to right, dark matter density, gas density, gas temperature and gas metallicity; Vogelsberger et al., 2014).

gelsberger et al., 2014). Their concordance with observational results is considered a key test to disentangle different cosmological models, structure formation scenarios, and the properties of the dark matter.

From the observational point of view, defining the moment when the first structures are sufficiently overdense to be defined as galaxy clusters is not trivial (for a review see Overzier, 2016). Traditionally, high redshift clusters are selected from optical/near-infrared large surveys, where galaxies are selected either by photometry or by the identification of their Balmer break (e.g. Gladders & Yee, 2005). X-ray surveys were also used to detect high redshift clusters (e.g., from the XMM-Newton Large Scale Structure survey, XMM-LSS; Pierre et al., 2004, 2011). This selection method is however limited to the most massive objects and to redshifts of $z \sim 1.5$ due

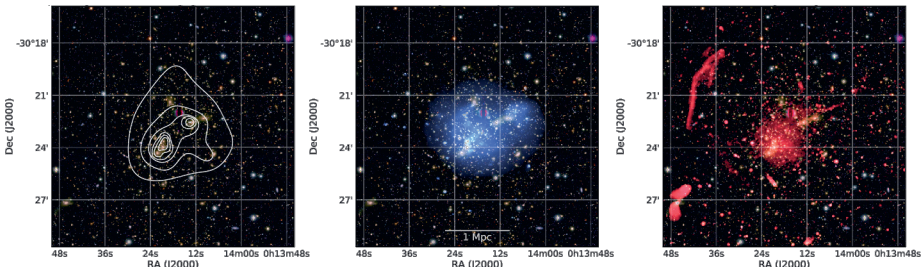

Figure 1.2: The galaxy cluster Abell 2744 in optical (left panel; Subaru *BRz* and contours of mass surface density, Medezinski et al., 2016), X-ray (central panel; Chandra 0.5–2.0 keV band in blue, Pearce et al., 2017) and radio (right panel; VLA 1–4 GHz band in red, Pearce et al., 2017). Image credit: van Weeren et al. (2019).

to surface brightness dimming. Surveys based on the Sunyaev-Zel'dovich (SZ) effect, through the spectral distortion of the Cosmic Microwave Background (CMB) photons traversing the ICM, have resulted to be very effective in detecting almost complete samples of high redshift clusters. The South Pole Telescope (SPT; Bocquet et al., 2019; Bleem et al., 2020; Huang et al., 2020), the Atacama Cosmology Telescope (ACT; Hilton et al., 2021) and the Planck satellite (PSZ2; Planck Collaboration et al., 2016) have found the largest number of clusters, reaching a redshift of $z = 2$. The epoch for the formation of the first massive structures is usually set at $z \sim 1.5 - 2.0$, i.e. 3–4 Gyr after the Big Bang. Nonetheless, virialized structures at higher redshift, with detected X-ray extended emission, have been observed (e.g., Andreon & Huertas-Company, 2011; Willis et al., 2013; Miller et al., 2018; Willis et al., 2020).

1.1.1. Merging Galaxy Clusters

The formation and growth of large-scale structures are processes that occur at any moment after the formation of the first massive structures, via accretion of matter along filaments in the cosmic web and/or via merger of (sub)clusters and galaxy groups (Press & Schechter, 1974; Springel et al., 2006). Cluster mergers are the most energetic events in the Universe since the Big Bang. These events release an energy up to 10^{64} ergs during a cluster crossing time, i.e. $\sim$ 1 Gyr (Markevitch et al., 1999). They can have a large impact on the cluster environment, affecting the galaxy distribution and evolution (left panel in Fig. 1.2; e.g. Golovich et al., 2019a), and changing the properties of the diffuse cluster plasma by means of turbulent motions, thermal discontinuities (such as shocks and cold fronts), and gas heating (middle panel in Fig. 1.2; see Markevitch & Vikhlinin, 2007, for a review). Moreover, a small fraction ($< 1\%$) of energy released during the merger is thought to be channelled into the acceleration of CRs

and magnetic field amplification (right panel in Fig. 1.2; see Brunetti & Jones, 2014, for a review). All these events make merging clusters unique laboratories where to address fundamental questions in astrophysics and in plasma physics. To investigate the physics of particle acceleration, the energy transport from the largest to the smallest scales, and the origin and topology of cosmic magnetic fields, a multi-frequency approach is required.

1.2. The Sunyaev-Zel'dovich effect

The Sunyaev-Zel'dovich effect (SZ; Sunyaev & Zeldovich, 1972) is a small distortion of the Cosmic Microwave Background (CMB) black body spectrum. It is caused by Inverse Compton (IC) scattering of the "cold" CMB photons that interact with the "hot" electrons in the ICM. As a result, the CMB intensity decreases (increases) at frequencies lower (higher) than 218 GHz. This change in the spectrum is proportional to the integral along the line of sight of the product of electron density and temperature, i.e. $y \propto \int_0^\infty n_e T_e dl$. This quantity is called the Compton parameter, and the SZ signal Y is obtained by integrating over the solid angle covering the cluster, i.e. $Y = \int_\Omega y d\Omega \propto 1/D_A^2 \int_0^\infty dl \int_A n_e T_e dA$ (with D_A the angular diameter distance and A the cluster area). Since this effect is a fractional change in the brightness of the CMB, it does not suffer from redshift dimming. Therefore, SZ-selected surveys are the most effective way to search for high redshift clusters, although the current surveys are limited by poor angular resolution (1 – 2 arcmin). An important property of the SZ signal is that it tightly correlates with the cluster mass (Arnaud et al., 2010):

$$Y_{500} D_A^2 \propto f_{\rm gas} M_{500}^{5/3} H(z)^{2/3}\,, \tag{1.1}$$

where the subscript 500 indicates the value within a radius that encompasses a density 500 times higher than the critical density of the Universe at the given redshift, $f_{\rm gas}$ is the fraction in mass of the ICM, and $H(z) = H_0\sqrt{\Omega_{\rm m}(1+z)^3 + \Omega_\Lambda}$ the Hubble parameter.

1.3. Thermal emission

The ICM represents the bulk of the baryonic content of the cluster mass. It is a hot ($T = 10^7 - 10^8$ K or $kT = 1 - 10$ keV) and rarefied ($n_e \sim 10^{-4} - 10^{-3}$ cm^{-3}) plasma, emitting X-ray radiation via thermal Bremsstrahlung emission (e.g. Forman et al., 1982), with emissivity as a function of frequency ν given by[2] $\varepsilon \propto n_e^2 T_e^{-1/2} \exp(-h\nu/kT_e)$. X-ray satellites, such as ROSAT and ASCA in the past, and Chandra, XMM-Newton and Suzaku more recently,

[2]Here, n_e and T_e are the electron number density and temperature, while h and k are the Planck and Boltzman constants, respectively.

have determined the density and temperature properties of clusters. These are done by means of spectral and surface brightness analyses and under the assumption of spherical symmetry (e.g. Markevitch & Vikhlinin, 2007). These observations revealed that the ICM mostly consists of fully ionised hydrogen and helium, plus a small fraction of highly ionised heavier elements at about a third of the solar abundance ($Z = 0.3\ Z_{\odot}$).

X-ray observations are important to determine the dynamical state of galaxy clusters. Relaxed (undisturbed) clusters have usually roundish and symmetrical shapes, with a central peak of X-ray emissivity. For the density distribution, a hydrostatic isothermal sphere is generally assumed (Cavaliere & Fusco-Femiano, 1976). This density profile results in the well-known β-model profile for the surface brightness (e.g. Jones & Forman, 1984), with a slope of $0.5 - 3\beta$ (with β being $\sim 2/3$; Arnaud, 2009). Relaxed clusters also tend to have a so-called cool core, i.e., a drop in the ICM temperature within the $0.1R_{500}$ radius, where R_{500} is the radius where the cluster density is 500 above the critical density of the Universe at that redshift. However, it is important to keep in mind that a spherical symmetrical morphology and a cool core do not necessarily imply the absence of dynamical activity. This can be the case of merger events seen along the line of sight, or sloshing events (e.g. Markevitch & Vikhlinin, 2007). Since relaxed clusters are usually brighter than disturbed systems, X-ray surveys host a larger fraction of cool core clusters compared to the Planck-SZ selected samples (Rossetti et al., 2017; Andrade-Santos et al., 2017; Lovisari et al., 2017). This is known as the cool core bias (Eckert et al., 2011).

1.3.1. Shock fronts

In the simple scenario of a merger between two clusters with masses M_1 and M_2, the merger velocity v at distance d is determined by (Sarazin, 2002):

$$v_{[\mathrm{km\,s^{-1}}]} \sim 3000 \left(\frac{M_1 + M_2}{10^{15}\,\mathrm{M}_{\odot}}\right)^{1/2} \left(\frac{d}{1\,\mathrm{Mpc}}\right)^{-1/2} \left[\frac{1 - (d/d_0)}{1 - (b/d_0)^2}\right]^{1/2}, \qquad (1.2)$$

where b is the impact parameter and d_0 is the initial cluster separation. As consequence of the merger, shock waves are generated and propagate perpendicularly to the merger axis. Shocks are revealed in X-ray observations as sharp discontinuities in the surface brightness profile. In this framework, the Chandra satellite, given its high angular resolution of $1''$, is the best instrument to date to investigate such features. Behind the shock, in the so-called *downstream* or *post-shock region*, the gas is compressed and heated proportionally to the Mach number of the shock ($\mathcal{M} = v_{\mathrm{shock}}/c_{\mathrm{s}}$; see Fig. 1.3). Given the typical temperature and density ahead of the shock

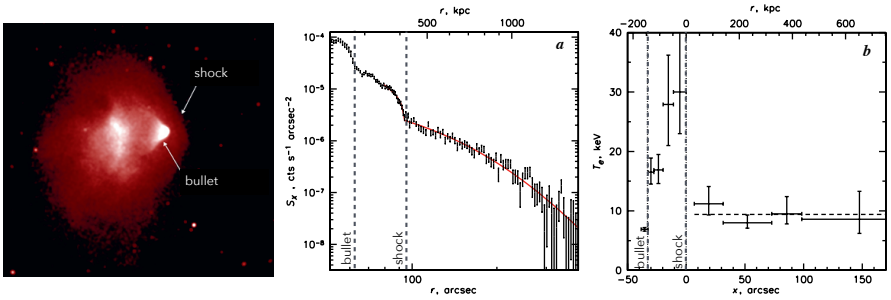

Figure 1.3: The Bullet galaxy cluster (1E 0657-56; Markevitch, 2006a). Left panel: 500 ks Chandra ACIS-I image in the 0.8–4 keV band. Middle panel: surface brightness profile covering the bullet and the shock front, highlighted by the dashed vertical lines; the red solid line represent a model for a shock front. Right panel: projected temperature profile in a narrow sector across the shock; the two vertical dashed lines show the boundaries of the cool bullet and the shock; the horizontal dashed line shows the average pre-shock temperature.

(the so-called *upstream* or *pre-shock region*), the sound speed[3] in clusters it is of the order of $\sim 1000\,\mathrm{km\,s^{-1}}$. Thus, the shocks in cluster mergers are expected to be only moderately supersonic, with Mach numbers of $\mathcal{M} \lesssim 3$. The shock Mach number ($\mathcal{M}$) is estimated using the Rankine-Hugoniot jump conditions (Landau & Lifshitz, 1959). Assuming a monatomic gas ($\gamma = 5/3$), then the temperature and density jumps detected in the cluster spectrum and surface brightness profile lead to:

$$\frac{T_{\rm post}}{T_{\rm pre}} = \frac{5\mathcal{M}^4 + 14\mathcal{M}^2 - 3}{16\mathcal{M}^2} \tag{1.3}$$

and

$$\frac{n_{\rm post}}{n_{\rm pre}} = \frac{4\mathcal{M}^2}{\mathcal{M}^2 + 3}\,. \tag{1.4}$$

From an observational point of view, detecting temperature jumps is more difficult because it requires the detection of a large number of photons. This is not always possible, especially in the pre-shock region which is usually faint (e.g. Bartalucci et al., 2014). However, determining $T_{\rm post} > T_{\rm pre}$ is necessary to define the nature of the discontinuity and to discriminate it from a cold front (see below).

1.3.2. Cold fronts

Cold fronts are sharp contact discontinuities which are in pressure equilibrium. They form at the boundaries of cold gas clouds moving through

[3]The sound speed is defined as $c_{\rm s} = \sqrt{\gamma kT/\mu m_{\rm p}}$

a hotter and less dense surrounding gas (ZuHone & Roediger, 2016). Simulations have shown that, during the cluster merger, the lower-entropy gas cores can be dense enough to resist the disruption by the shocks and stay attached to their host dark matter. Moreover, the gas pressure appears to be continuous across the discontinuity. Observations of these sharp discontinuities have been possible thanks to the extremely high resolution of the Chandra satellite. These observations enable the study of the physical properties of the cluster plasma, the mean free path of electrons and ions, and thermal conduction and flow instabilities. One of the textbook example of X-ray observations of a merging cold front is seen in the Bullet cluster (1E 0657-56; Markevitch, 2006a, see Fig. 1.3). Unlike shock fronts, these discontinuities can be also observed in relaxed clusters and they are the signature of recent minor merger and related gas sloshing event in the cluster core (e.g. Perseus cluster, Simionescu et al., 2012; Walker et al., 2018).

1.3.3. Turbulence

During a merger event, a non-negligible amount of turbulence is injected in the ICM. The degree of turbulence can be quantified by the Reynolds number, which is defined as the ratio between the inertial and viscous forces (i.e. $\mathrm{Re} = v_L L/\nu$, where v_L and L are the velocity and injection scale of the turbulence, and ν the plasma viscosity). Turbulence is dissipated throughout the cluster volume, propagating from large to small scales. Given typical ICM values, and assuming that the largest scale for the injected turbulence is the size of the cluster core, theories predict an effective Reynolds number of $\mathrm{Re} \sim 10^3$ (Brunetti & Jones, 2014). Including the kinetic and magnetic instabilities and considering the weakly collisional nature of the ICM, the Reynolds number can reach much larger values.

ICM turbulence is usually quantified via numerical simulations (e.g. Ryu et al., 2008; Miniati & Beresnyak, 2015; Vazza et al., 2017). Recently, direct evidence for ICM turbulence has been studied in the Perseus Cluster, thanks to Hitomi (Hitomi Collaboration et al., 2016; ZuHone et al., 2018), and in the Coma Cluster, thanks to Chandra Zhuravleva et al. (2019). These works point to large Reynolds numbers ($\mathrm{Re} > 10^3$), suggesting that the ICM is highly turbulent.

1.4. Non-thermal emission

Galaxy clusters display a large variety of radio emission from non-thermal synchrotron radiation. Radio galaxies are a particular class of active galactic nuclei (AGN; Urry & Padovani, 1995), and are the most common sources of synchrotron emission. Unlike those observed in isolated environments, cluster radio galaxies display peculiar morphologies. As they move in the

cluster potential well, their jets are not symmetric but they bend in the opposite direction of the motion due to ram pressure (Miley, 1980). They are therefore called *head* (HT), *narrow-angle* (NAT) and *wide-angle* (WAT) tails, depending on the bending angle of the radio jets, and can be used to trace the cluster dynamics. The morphology of cluster radio galaxies can be strongly affected by a merger event, causing additional changes to their shapes (e.g. IC 711 in Abell 1314, see Wilber et al., 2019).

In merging galaxy clusters, diffuse radio emission[4], extending from 500 kpc up to 1-2 Mpc and not directly associated with galaxies, is also detected. These are referred to as *radio relics* and *radio halos* (Sect. 1.4.1 and 1.4.2, respectively; see Brunetti & Jones, 2014; van Weeren et al., 2019, for theoretical and observational reviews). The observations of these radio sources proves the presence of relativistic particles, i.e. cosmic rays (CRs) with Lorentz factor $\gamma_L \sim 10^4$ or GeV energies, and magnetic fields in the ICM (see also Sect. 1.5). A fundamental problem arises for the origin of the CRs[5] associated with these diffuse sources. The typical distribution of CRs follows a power law, i.e. $N(E) = N_0 E^{-\delta} dE$, with the spectral slope $\alpha = (1-\delta)/2$ reflecting the physics of the particle acceleration and the electron energy losses. The characteristic lifetime of relativistic particles is set by the combination of synchrotron and inverse Compton (IC) energy losses, according to (e.g. van Weeren et al., 2011b):

$$t_{[\mathrm{yr}]} \approx 3.2 \times 10^{10} \frac{B^{1/2}}{B^2 + B^2_{\mathrm{CMB}}} [(1+z)\nu]^{-1/2} \ , \tag{1.5}$$

where B is the cluster magnetic field, $B_{\mathrm{CMB}} = 3.25(1+z)^2\ \mu$Gauss is the equivalent magnetic field strength of the CMB, ν is the observing frequency in MHz and z is the source redshift. In clusters, where the relativistic particles have energies up to ~ 1 GeV, the typical age of the relativistic particles results to be $t < 10^8$ yr. This lifetime is much shorter than the time needed to transport these particles within the cluster volume, i.e. $t \sim 10^9$ yr. This is also known as *diffusion problem*. Therefore, the ultra-relativistic particles in radio halos and radio relics cannot be simply associated with output from AGN or galactic winds, but they need to be continuously (re-)accelerated in-situ (Jaffe, 1977).

[4]Additional diffuse radio emission in cool-core clusters are sometimes detected, on smaller scales (i.e. $\lesssim 500$ kpc, see Giacintucci et al., 2017). These are called *mini-halos*, and will not be described in this thesis.

[5]In this thesis, we refers to relativistic electrons (i.e. CRe) as the primary component of the CR populations in galaxy clusters producing diffuse radio emission. Relativistic protons (CRp) are difficult to be observed directly, and would generate γ-ray emission due to $p+p$ decay, which has not been detected with the Fermi-LAT satellite (Ackermann et al., 2016).

1.4.1. Radio relics

Radio relics (Fig. 1.4) are large, from 500 kpc up to 2 Mpc, diffuse radio sources located in the cluster outskirts (Vazza et al., 2012b). They have elongated, usually arc-like, shapes and are generally co-spatial with the shock discontinuities detected in the X-ray band. For this reason, they are also called *radio shocks* (van Weeren et al., 2019). Radio relics are found to be strongly polarised at frequencies above $\sim$ 1 GHz (from 20% up to 60%, e.g. Ensslin et al., 1998; van Weeren et al., 2010), with the polarisation electric vectors orientated perpendicularly to the shock surface. Recent GHz observations at high resolution have shown that these sources have filamentary structures (e.g. Abell 2256, Owen et al., 2014; 1RXS J0603.3+4214, Rajpurohit et al., 2018a; CIZA J2242.8+5301 Di Gennaro et al., 2018). The origin of this filamentary morphology is still not fully understood. It has been proposed that it can be due to the complex shape of the shock surface (Vazza et al., 2012a; Skillman et al., 2013) or because of changes in the magnetic field (Wittor et al., 2019), or a combination of these two effects. A particular class of radio relics are the so-called *double radio relics* (e.g. Roettiger et al., 1999, right panel in Fig. 1.4). These are the result of a cluster merger that occur very close to the plane of the sky, where a pair of shock waves are generated at same time at the core passage. As they do not suffer from geometrical projection effects, double radio relics are useful tools to constrain the merger parameters and dynamics (van Weeren et al., 2011a; Molnar & Broadhurst, 2017; Golovich et al., 2019b).

Radio relics are characterised by steep integrated radio spectra, with $\alpha_{\rm int} < -1$. The power-law shape of their spectra has been observed over a wide frequency range, from hundreds MHz up to tens GHz (Rajpurohit et al., 2020; Loi et al., 2020). At the outermost edge of the relic, where the shock is located, a flatter spectral index is observed, with $\alpha \sim -0.8$. The spectral index steepens towards the cluster centre, reaching values $\alpha \lesssim -1.5$. This steepening in the post-shock region is caused by synchrotron and inverse Compton energy losses.

All the characteristics mentioned above point to (re-)acceleration of CRs and compression and amplification of magnetic fields, due to the merger-induced shock (Brunetti & Jones, 2014; Donnert et al., 2018), to explain the origin of radio relics. Models for the radio relic population by Nuza et al. (2012) predict that the radio relic occurrence rate should increase with redshift, that the most massive clusters should have the highest probability to host relics, and that they should be distributed closer to the cluster centre than those observed at $z = 0$ (Vazza et al., 2012b).

The two main mechanisms invoked to explain the origin of radio relics are the diffusive shock acceleration (DSA; Blandford & Eichler, 1987) and the re-acceleration of fossil plasma (Markevitch et al., 2005).

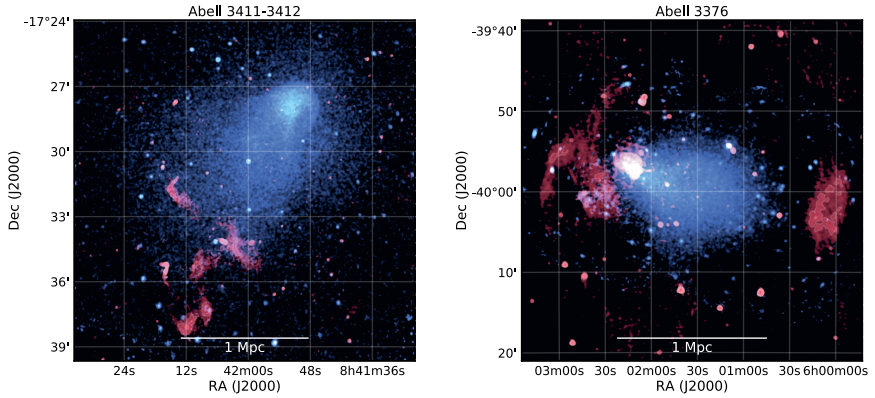

Figure 1.4: Examples of radio relics. Left panel: the single relic in Abell 3411-3412 (GMRT 325 MHz, van Weeren et al., 2017a; Andrade-Santos et al., 2019). Right panel: the double relic in Abell 3376 (GMRT 317 MHz, Kale et al., 2012; Urdampilleta et al., 2018). The radio emission is shown in red colour, while in blue there is the thermal X-ray emission (Chandra 0.2–2.0 keV and XMM-Newton 0.3–2.0 keV, respectively). Images are taken from van Weeren et al. (2019).

Diffusive shock acceleration (DSA) mechanism

Diffusive shock acceleration is a first-order Fermi acceleration mechanisms. According to this, particles from the thermal pool scatter upstream and downstream from the shock due to magnetic inhomogeneities. At each crossing, particles gain some energy until they become relativistic enough to produce synchrotron radiation. An important prediction of this mechanism is that the integrated spectrum of the accelerated CRe follows a power-law distribution, which depends only on the shock Mach number:

$$\alpha_{\rm int} = \frac{\mathcal{M}^2 + 1}{\mathcal{M}^2 - 1} \,. \tag{1.6}$$

Comparing the shock Mach number measured from X-ray and radio observations is one of the key tests for the DSA mechanisms. If the lifetime of the shock and the electron diffusion time are much longer than the electron cooling time, the integrated spectral index relates with the injection spectral index according to $\alpha_{\rm inj} = 0.5 + \alpha_{\rm int}$ (Kardashev, 1962). Nonetheless, in several cases deviations from the injected-integrated spectral indices relation (e.g. van Weeren et al., 2012, 2016; Hoang et al., 2017) and discrepancies between the X-ray and radio Mach numbers (e.g. Akamatsu et al., 2017) are observed. A suggested explanation for this latter issue is that, unlike X-ray observations, radio observations are sensitive to the "high-value tail" of the shock Mach number distribution (e.g. Wittor et al., 2017)

The stronger issue with the DSA mechanisms is that, to explain the surface brightness observed in radio relics, high acceleration efficiencies ($\eta \gtrsim 10\%$) are required. While this is not a problem for high Mach numbers (like for shocks produced in the supernova remnants, $\mathcal{M} \sim 10^3$), this appears particularly unrealistic for cluster shocks ($\eta \lesssim 1\%$, Kang & Ryu, 2013).

Re-acceleration scenario

The challenge of the low acceleration efficiency can be solved if we consider a source of pre-existing accelerated plasma, instead of the thermal pool. In this case the particles are already relativistic, therefore even a weak shock (e.g. Di Gennaro et al., 2019; Andrade-Santos et al., 2019) can re-accelerate them and produce strong radio emission. Since the physics in act is still DSA, apart from the change in the initial seed particles, the spectrum of the ultra-relativistic particles is still described by Eq. 1.6.

The sources for this pre-existing plasma are usually found in cluster radio galaxies. Connections between lobes of radio galaxies and radio relics have been observed (e.g. Shimwell et al., 2015; van Weeren et al., 2017a,b; Di Gennaro et al., 2018). Numerical models have been successful in reproducing the observed radio flux density and volume-integrated spectral index, at least for the radio relics in 1RXS J0603.3+4214 and CIZA J2242.8+5301 (Kang & Ryu, 2011; Kang et al., 2012, 2017).

1.4.2. Radio Halos

Radio halos are large-scale (1–2 Mpc) diffuse radio sources located in the cluster centre (van Weeren et al., 2019, Fig. 1.5). They have roundish shapes, which follow well the X-ray emission from the ICM. Recent deep and high-resolution observations have shown that these sources might not be completely smooth, but they can be characterised by filamentary shapes (Botteon et al., 2020). Unlike radio relics, radio halos are not polarised. This is probably due to poor angular resolution, which results in beam depolarisation. Expected polarisation values of 15–35% have been predicted for high-resolution observations using magneto-hydrodynamical simulations (Govoni et al., 2013).

Radio halos are characterised by steep spectral indices, with values ranging from $-1.3 < \alpha < -1.0$ (Giovannini et al., 2009; Feretti et al., 2012; van Weeren et al., 2019). The spectral index is usually rather constant across the halo, although a few halos display inhomogeneities on small scales (Orrú et al., 2007; Shimwell et al., 2016). For a few objects with observations at several different frequencies, curved spectra have been observed (e.g. Thierbach et al., 2003). Last but not least, the discovery of ultra-steep spectrum radio halos (USSRH; Brunetti et al., 2008; Dallacasa

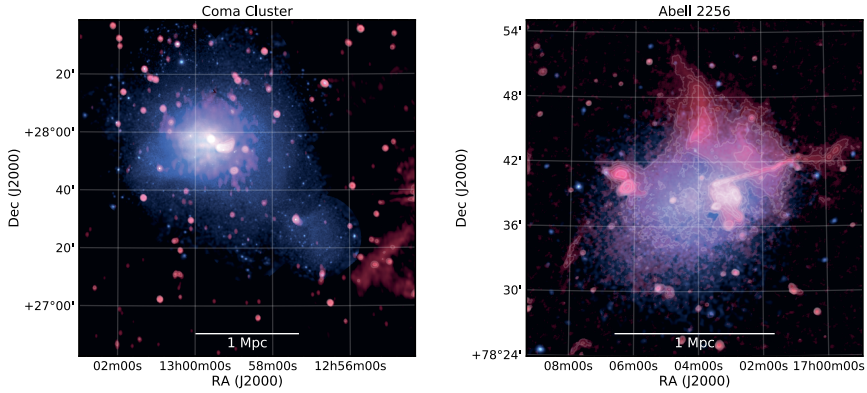

Figure 1.5: Examples of radio halos. Left panel: Coma cluster (WSRT 352 MHz, Brown & Rudnick, 2011). Right panel: Abel 2256 (LOFAR 120–170 MHz, van Weeren et al. in prep). The radio emission is shown in red colour, while in blue there is the thermal X-ray emission (XMM-Newton 0.4–1.3 keV). Images are taken from van Weeren et al. (2019).

et al., 2009; Wilber et al., 2018) has provided compelling information on the underlying acceleration mechanism.

Several studies have linked the radio emission from halos to the X-ray emission of the ICM. In particular, the most powerful radio halos have been found in the most massive and X-ray luminous clusters (e.g. Cassano et al., 2013). Moreover, a clear bi-modality between merging and relaxed cluster is observed, with the former hosting radio halos and the latter showing no radio emission.

Re-acceleration scenario

This observed bi-modality suggests that the dynamical state of the cluster should be connected with the formation mechanism of radio halos (Brunetti et al., 2001; Petrosian, 2001). The general idea is that the large scale MHD turbulence produced during a cluster merger is transferred to smaller and smaller scales (Brunetti & Jones, 2014). Turbulence on small scales can result in second-order Fermi processes, where particles scatter due to magnetic inhomogeneities. Since the particle motion is random in the ICM, a slight net gain of energy occurs after many scatterings. A challenge for this scenario is that it requires the presence of mildly–relativistic electrons in the ICM, as MHD turbulence is not efficient enough to accelerate electrons from the thermal pool. This mechanism satisfies the diffusion problem mentioned in Section 1.4, the presence of radio halos in disturbed systems and the correlation between the halo radio power and the cluster mass. It also explains the observation of USSRHs, where

the radiative energy losses are stronger than the re-acceleration processes (Cassano & Brunetti, 2005; Cassano et al., 2006). A consequence of this model is that radio halos should be transient events in the cluster life-time.

In the last decade, models based on the turbulent re-acceleration theory have been developed to investigate the occurrence rate of radio halo as a function of cluster mass and redshift (Cassano et al., 2010a, and references therein). These models predict that the detectable fraction of clusters at high z hosting halos should decrease at GHz frequencies, and that, for a given mass, these radio halos are expected to have steeper radio spectral indices than their low-z counterparts (i.e. $\alpha < -1.5$). This latter prediction is due to the IC energy losses which limit the maximum energy of the accelerated electrons (Cassano et al., 2006). Before this Thesis, only few single objects have been observed at redshift above 0.6 ("El Gordo" at $z = 0.87$, Lindner et al. 2014; PLCK G147.3-16.6 at $z = 0.65$, van Weeren et al. 2014; PSZ2 G099.86+58.45 at $z = 0.616$, Cassano et al. 2019).

Secondary models

Secondary products of inelastic hadronic collisions between CRp and thermal protons in the ICM (i.e. p+p collisions) would also be able to generate the electrons and positrons responsible for the radio halo emission (e.g. Blasi & Colafrancesco, 1999). This mechanism solves the diffusion problem and the connection between the radio and the X-ray emission. The main issue of this scenario is that it would predict diffuse radio emission from both disturbed and relaxed clusters, which has not been observed (Cassano et al., 2013). Moreover, these collision would also produce γ-ray emission, whose detection is still missing (e.g. Ackermann et al., 2010b, 2014, 2016; Prokhorov & Churazov, 2014a; Brunetti et al., 2017).

1.5. Cluster magnetic fields

Magnetic fields are ubiquitous in the Universe, from stars to the largest structures (Klein & Fletcher, 2015). Although not directly observable, in clusters they are thought to play key roles not only for particle (re-)acceleration, but also to regulate AGN feedback, thermal conduction, and the ICM pressure budget (Carilli & Taylor, 2002).

There are several methods to retrieve the magnetic field strengths in clusters (Carilli & Taylor, 2002; Govoni & Feretti, 2004a). These studies lead to volume-averaged strengths of a few μGauss. A common method is to use the Faraday Rotation Measure (RM) from background/inside polarised sources. When a linearly polarised emission passes through a magnetised plasma, it experiences a phase shift $\Delta\chi$ of its left and right circularly polarised components. This results in a rotation of the polarisation plane at higher (lower) wavelengths λ (frequencies ν), $\Delta\chi = \mathrm{RM}\lambda^2$.

The Rotation Measure is defined as the integral along the line of sight L of the product of the electron density and the parallel component of the magnetic field, i.e. RM $\propto \int_0^L n_e B_\parallel dl$. Therefore, if n_e is known (i.e., from X-ray observations), $B_\parallel$ from the ICM can be estimated by measuring RM from several polarised sources located inside and/or background the cluster (Bonafede et al., 2010a). In relaxed clusters, where a β model can be assumed to describe the electron density profile, central magnetic fields of 1–15 μGauss have been estimated with decreasing values in the cluster outskirts. Several issues arise with this method (Johnson et al., 2020). First, the number of background polarised sources per cluster is usually low (Rudnick & Owen, 2014). At high redshift, this number is even lower, and therefore applying this method is more challenging. Furthermore, determining the location of embedded sources is difficult, and quantifying the effect of the interaction between the ICM and the radio galaxy plasma on the measured RM is not straightforward. Secondly, since RM is an integrated value, it collects the signal from all the material along the line of sight. It is therefore difficult to separate the contribution of foreground layers, e.g. the Galactic plane (Oppermann et al., 2015). In this case, the RM-Synthesis technique (Brentjens & de Bruyn, 2005) is more sensitive to multiple Faraday screens. Thirdly, it is hard to characterise the inhomogeneities in the magnetic field structures and the turbulent spatial scales in the ICM. Investigating all these most common issues, Johnson et al. (2020) derived an accuracy for the magnetic field strength from Rotation Measures of a factor ~ 3.

Another method to obtain the cluster magnetic field strength is by comparing the synchrotron (which is proportional to B^2) and the X-ray emission in the hard band (i.e. > 10 keV). The latter is caused by IC scattering between CMB photons and ICM electrons, and therefore proportional to $B_{\rm CMB}$. The main challenge with this method is that the cluster X-ray emission at > 10 keV is difficult to detect. Only upper limits on the magnetic field strengths have been obtained so far by this method.

Finally, equipartition arguments have also been used in the past to determine cluster magnetic field strengths (Feretti et al., 2012).

1.5.1. Origin and amplification of cluster magnetic fields

One of the still open question in astrophysics is how the Universe we observe now is magnetised on the large scales. The general idea is that initial "seeds" of magnetic field get amplified as the Universe expands. It is still unclear where the magnetic field seeds come from. Two main scenarios have been proposed to address the origin of these seeds (see Subramanian, 2016, for a theoretical review). The first one assumes that magnetic field seeds have *primordial* origins. They are thought to be generated during the inflationary phase of the Universe, i.e. much before galaxy clusters form as

gravitationally bound systems. In this case, perturbations due to primordial magnetic fields will induce temperature and polarisation anisotropies, which should be detectable in the CMB. Based on measurements of the CMB, it has been found that an initial magnetic field strength of $B_0 \lesssim 1$ nGauss should permeate the entire Universe (Dolag et al., 2005; Planck Collaboration et al., 2016). Another possibility is that these seeds are generated around $z \sim 2-3$ from *astrophysical* objects, i.e. galactic winds, AGN, and/or starbursts. The impact of these objects on the cluster medium is observed, for instance, in the large-scale metallicity distribution (e.g. Baumgartner & Breitschwerdt, 2009; Biffi et al., 2018; Simionescu et al., 2019; Urdampilleta et al., 2019). It is therefore plausible that these objects are also able to inject magnetic field seeds in clusters, which can reach initial values of $B_0 \sim 0.1$ μGauss (Dolag et al., 2005).

In both scenarios, the initial magnetic field seeds are expected to be amplified during structure formation (see Donnert et al., 2018, for a recent review). Considering only the amplification due to gravitational collapse without any "external" effects, the magnetic field amplification is expected to be extremely slow, and would not reach the $\sim \mu$Gauss level we currently measure in galaxy clusters. The main mechanism for magnetic field amplification in galaxy clusters is the *small-scale dynamo* (Kraichnan & Nagarajan, 1967; Goldreich & Sridhar, 1997; Schekochihin & Cowley, 2007). The general idea is that merger-induced kinetic turbulent energy is transferred to magnetic energy, which stretches and folds the pre-existing magnetic field lines and locally amplifies the magnetic fields. This process takes several eddies turnover times, i.e. several Gyrs (Beresnyak & Miniati, 2016).

1.6. X-ray and radio instruments

In the last decades, the synergy of radio telescopes and X-ray satellites has provided enormous advances in the understanding of the physics of galaxy clusters, spanning from the thermal to non-thermal phenomena.

Since the launch of the Chandra X-ray satellite in the late 1990s, impressive details in the ICM have been observed. The satellite, which orbits about 140,000 km above the Earth's atmosphere, is formed by four pairs of concentric mirrors which focus X-ray photons in the energy range of 0.1–10 keV to the High Resolution Camera (HRC) and the Advanced CCD Imaging Spectrometer (ACIS). The high accuracy of the mirrors results in the impressive resolution of $< 1''$ (corresponding to less than 1 kpc at $z < 0.05$), and therefore Chandra is the optimal instrument to detect sharp edges in clusters. On the other hand, the effective area of Chandra is rather small, 800 and 400 cm^2 at 0.25 and 5 keV respectively. Regarding effective area, XMM-Newton is a better instrument, with an effective area of about 1500 cm^2 at 1 keV. This instrument, however, looses in resolution

(about 15″).

The study of the large-scale non-thermal components has been historically carried at GHz frequencies. At these frequencies, the Karl-Jansky Very Large Array (VLA), located in New Mexico (US), represents one of the best instruments. This radio interferometer is composed by 27 parabolic dishes of 25 meters diameter which can move on a Y-shaped rail track. The option to move the antennae allows the interferometer to have four different configurations (A, B, C and D) which are sensitive to different angular scales. The observing frequency coverage spans from 0.74 to 50 GHz, which is divided in ten observing bands (e.g. the L- and S-bands cover the 1–2 and 2–4 GHz frequency bands, respectively). The angular resolution depends on both the array configuration and the observing frequency, spanning from subarcsec to the arcmin. The presence of steep-spectra radio emission has pushed the observations in the $\sim$ 100 MHz regime. The Giant Metrewave Radio Telescope (GMRT), located in India, consists in 30 parabolic wire-made dishes of 45 meters diameter which observe from 150 MHz to 1.4 GHz. The interferometer has been recently upgraded from a narrow-band to a wide-band system, significantly improving the noise levels. Given its location, the GMRT can also observe part of the southern sky (from -53° to $+90^\circ$). The Low-Frequency Array (LOFAR) is the largest interferometer to-date. It is mostly located in the Netherlands, plus additional stations placed in several countries in Europe. Contrary to the VLA and GMRT, this interferometer is formed by dipoles which collect radio waves that are then combined electronically to form a station beams using the *aperture phase array technique*. This technique also allows one to simultaneously observe different part of the sky, although it requires high computing power. LOFAR consists of two sets of antennas in each station, the Low Band Antennas (LBA, 10–90 MHz) and the High Band Antennas (HBA, 110–240 MHz). At such low frequencies, the distortions of the radiation due to the ionosphere is limiting for high-resolution imaging, and needs to be corrected with "local" direction-dependent calibration. Novel algorithms attempt to solve this issue, and now the realisation of the deepest and highest resolution images at MHz frequencies is possible. Particularly, the LOFAR Two-Meter Sky Survey (LoTSS) has reached a sensitivity of less than 100 μJy beam^{-1} and a resolution of 5″. Its combination with the LOFAR Low-frequency Sky Survey (LoLSS) aims to unveil the low energetic population of electrons in the northern sky.

1.7. This Thesis

This thesis is aimed to understand the origin of the diffuse radio emission in merging galaxy clusters, and its connection with the disturbed thermal gas. To address these topics, high-resolution and high-sensitivity radio and X-ray observations are required. The thermal ICM is investigated

using observations from the Chandra and Suzaku X-ray satellites. The non-thermal radio emission is studied by means of large radio interferometers, i.e., the Very Large Array (VLA), the Giant Metrewave Radio Telescope (GMRT) and the Low-Frequency Array (LOFAR).

The main questions addressed in this thesis are:

- How are the particles accelerated to ultra-relativistic energies at radio relics (Chapter 2)?
- How is the shock strength related with the presence of diffuse radio emission (Chapter 3)?
- What is the occurrence rate of diffuse radio emission at the epoch of the formation of the largest scale structures (Chapter 4)?
- How is large-scale magnetic field compressed and amplified by shocks (Chapter 5)?
- Are re-acceleration models also valid at the time when the first large structures formed (Chapter 6)?

In this context, observations of double radio relics are crucial to investigate the properties of merger-induced shocks, as they reflect merger events close to the plane of the sky and, therefore, minimise the effect of geometrical projection. Survey at low-frequencies are required to create a sufficiently large sample of high-z clusters, to determine the radio halo occurrence rate and its evolution.

In **Chapter 2**, a deep 1–4 GHz Very Large Array (VLA) study is carried out of the merging galaxy cluster CIZA J2242.8+5301 (van Weeren et al., 2010). We investigated the particle acceleration mechanisms that generate the two relics in this system, and attempted to explain the filamentary morphology of the northern relic. The VLA data were combined with existing GMRT (van Weeren et al., 2010) and LOFAR (Hoang et al., 2017) observations. The results from the radio analysis are compared with the shock properties reported in the literature (Ogrean et al., 2014; Akamatsu et al., 2015). The spectral index analysis and modelling suggest that the three-dimensional shape of the shock cannot be neglected, and we underlined some tensions for the DSA scenario for the particle acceleration. I also detected a clear connection between the southern relic and a tailed radio galaxy. This supports the idea that the fossil plasma of the radio tail is re-accelerated by the shock wave, as we also suggest with re-acceleration modelling. High-resolution mapping of other tailed radio galaxies and patches of diffuse emission also supports a scenario where fossil plasma is revived by the merger event.

In **Chapter 3**, the thermal properties of the double shock in the merging galaxy cluster ZwCl 0008.8+5215 are studied by means of deep Chandra

and Suzaku observations. In this system, a double radio relic was previously found by van Weeren et al. (2011b). The deep Chandra observations confirmed the presence of a cold front, with a morphology resembling that in the Bullet cluster. Ahead of it, a shock discontinuity was detected. Interestingly, the radio relic located at this position traces only partly the X-ray detected shock. On the opposite side, where the larger and brighter relic is found, no clear thermal discontinuity was detected. The comparison between thermal and non-thermal properties of the system strongly suggests that the origin of the radio relics is due to re-acceleration of fossil plasma.

In **Chapter 4**, we investigate the occurrence of diffuse radio emission at the epoch of cluster formation. LOFAR observations of a Planck Sunyaev-Zel'dovich selected sample of galaxy clusters were used to search for large-scale diffuse radio emission. We found that radio halos in massive, distant clusters are common in our sample, with an occurrence fraction of about 50%. The radio luminosities from radio halos, in spite of the strong Inverse Compton losses at high redshift, are comparable to those measured in nearby clusters in the same mass range. This also indicates that these clusters have magnetic field strengths that are similar to those in nearby clusters. Therefore, we propose a fast magnetic field amplification during the first phases of cluster formation.

In **Chapter 5**, deep 1–4 GHz VLA observations were used to investigate the polarisation properties of the northern relic in CIZA J2242.8+5301. In order to do so, we used the QU-fitting approach assuming a (de)polarisation model to fit directly the Stokes I, Q and U fluxes obtained from each channel of the observing band. We detected, for the first time, the filamentary shape of the relic also in polarised light, suggesting it is tracing the magnetic structure of the radio shock. We found increasing intrinsic polarisation fraction in the relic post-shock region. This could be explained by complex geometrical projection and/or the relic's shape. Finally, strong Rotation Measure fluctuations are found within and outside the cluster. Since the cluster is very close to the Galactic place, it is unclear how much of these fluctuations are due to the ICM or the the Galaxy.

In **Chapter 6**, observations with the upgraded GMRT (uGMRT) in Band 3 and 4 (250–500 and 550-900 MHz, respectively) were conducted to investigate the spectral index properties of the distant radio halos presented in Di Gennaro et al. (2021a). This is the first time that low-frequency observations were followed-up at higher frequencies. We find extended diffuse radio emission at the uGMRT frequencies in five of the nine clusters in the sample. These are also the most massive systems in our sample, with masses $M = 6-8\times10^{14}$ $M_{\odot}$. For these, an average global spectral index between -1 and -1.4 has been estimated. For the non-detected radio halos, we obtain an upper limit on the spectral indices of $\alpha < -1.5$. This supports

the scenario where only the most energetic (i.e. massive) mergers are able to accelerate particles at $\nu > 600$ MHz.

1.8. Future prospects

Despite the progresses achieved in the last decades, there are several crucial open questions regarding the physics of particle acceleration, the origin of cosmic rays, the evolution of the merger energetics, the amplification of magnetic fields, and the growth of cluster's baryonic content. In this framework, the development of new radio (LOFAR, MWA, SKA, ASKAP, MeerKAT) and X-ray (eROSITA, Athena) facilities, as well as the upgrade of the previous generation of radio telescopes (VLA, GMRT, WRST), is crucial to improve our knowledge of the thermal/non-thermal physics in galaxy clusters. This is extremely important both at low and high redshift.

To date only incomplete samples of galaxy clusters are available at $z > 0.6$, and they are restricted to the most massive systems. For this reason, comparisons with cosmological simulations are difficult. The work presented in Chapter 4 (Di Gennaro et al., 2021a) represents the first crucial step towards the characterisation of the non-thermal emission in distant galaxy clusters. The launch of the X-ray satellite eROSITA (Merloni et al., 2012) is very timely in this context, as its main goal is to test the current Cosmology observations of distant galaxy clusters. The eROSITA all-sky survey (eRASS) is expected to detect up to several hundreds of galaxy clusters at redshifts above 0.6 (Merloni et al., 2012). The constantly increasing sky area observed by the LOFAR Two-Meter Sky Survey (LoTSS; Shimwell et al., 2017, 2019) will allow an immediate follow up of these systems, searching for diffuse radio emission. Moreover, new powerful radio telescopes in the Southern Hemisphere (e.g. ASKAP and MeerKAT) are close to be fully operational. They will observe an almost unexplored part of the sky, where large mass-selected sample of clusters are already available (e.g., from the SPT survey; Ebeling et al., 2010; Bleem et al., 2020). Combining these X-ray and radio observations will allow the investigation of the morphological and spectral properties of the diffuse radio emission, and the comparison with the cluster dynamical state. In particular, measuring spectral index in distant radio halos will be the key test for the validation of the re-acceleration turbulent scenario (Cassano et al., 2006). Observations with the upgraded GMRT (uGMRT) at $\nu \sim 600$ MHz and with LOFAR LBA at $\nu < 100$ MHz will provide the sensitivity and the resolution for such studies (Di Gennaro et al., in prep).

The recent high-resolution (arcsecond) observations at GHz frequency have challenged the acceleration mechanisms aimed to explain radio relics (Owen et al., 2014; Di Gennaro et al., 2018; Rajpurohit et al., 2018a). Tensions have been found regarding the exact location of the (re-)acceleration site. Observations at $\sim$ 100 MHz frequency at the same high resolution

of VLA are required to investigate such issues. The International LOFAR Telescope (ILT), which contains stations from several European countries, together with the VLA will be able to study the spectral index coherence along the relic length. This is crucial to understand whether those filament are tracing the complex shape of the shock surface. Moreover, the understanding of merger-induced shocks will be boosted up by the launch (expected around 2030) of the Athena X-ray satellite (Nandra et al., 2013), whose energy resolution and collecting area will be revolutionary to directly measure turbulence in galaxy clusters.

The magnetic field properties at radio relics are also still poorly known. Only few bright relics have been studied in polarised light, and the origin of their filamentary structures is a mystery. It remains unclear whether the observed polarisation properties are peculiar cases or whether they apply to the entire population of relics. The complex Faraday structure of these sources and of the foreground layers require wide-band observations at GHz-frequency, to avoid depolarisation. VLA and MeerKAT observations can be used to investigate single objects in detail. Moreover, surveys aimed to observe a large number of polarised sources (e.g. POSSUM) are necessary to improve the statistical results on the Faraday Rotation Measurements in clusters. The SKA precursors, such as LOFAR and ASKAP, will allow the study of the cluster magnetic field topology in great detail.

Finally, theoretical models to connect the morphologies of radio tails in galaxy clusters to the merger-induced shock waves have been recently developed (Jones et al., 2017; O'Neill et al., 2019). High-resolution observations of the tail-relic interplay are essential to validate such models, and to determine the re-acceleration time scale of magnetised plasma swept up by a shock wave.